Infrared constrained equilibria and application to snowflake divertor studies

J.T. Wai [a], P.J. Vail [a], A.O. Nelson [a], Z.A. Xing [b], C. Lasnier [c], E. Kolemen [a,b,*]

[a] *Princeton University, Princeton, NJ, USA*
[b] *Princeton Plasma Physics Laboratory, Princeton, NJ, USA*
[c] *Lawrence Livermore National Laboratory, Livermore, CA, USA*

ABSTRACT

One of the challenges of the snowflake divertor (SFD) configuration is finding a reliable means of reconstructing the magnetic field geometry in the divertor. Since the SFD (and other advanced divertors) have multiple field nulls, there is a large region with shallow flux gradients that is difficult to resolve accurately using external diagnostics. In this work we present a technique that uses heat flux measured by the infrared television (IRTV) camera to improve SFD reconstruction. This is relevant for purposes of control, since the SFD is topologically unstable and requires active feedback on the shape [E. Kolemen, et. al., Nucl. Fusion, 58, 6 (2018)], and analysis, since reconstructions provided by other algorithms such as EFIT [L. Lao, et. al., Nucl. Fusion, 25, 11 (1985)] can mis-characterize the shape and even the snowflake type (plus or minus). The technique identifies the spatial position of the two x-points located in the SFD based on characteristics of the heat flux such as the strike point location and power distribution. The inferred x-point positions are then used as a constraint in fitting new equilibria using the TokSys suite of software. This procedure is applied to ~800 DIII-D SFD timeslices and reduces the summed strike point errors from an average 9.4 cm to 0.9 cm. The newly-created x-point constrained equilibria are compared to kinetic reconstructions and an average 16% reduction in the edge current is observed. This is correlated via a simple linear relationship to the shape constraints. Other changes in the pedestal structure are observed, but more work must be done to incorporate the IRTV constraint directly into kinetic solvers to obtain integrated solutions.

1. Introduction

Mitigating the power-exhaust onto plasma-facing components (PFCs) is one of the critical challenges that must be addressed to successfully achieve the tokamak fusion reactor concept. The present vision for the plasma-material interface is a magnetic configuration known as the axisymmetric x-point divertor in which plasma which has escaped confinement travels along open magnetic fieldlines to thermally and mechanically hardened surfaces. The divertor configuration is intended to mitigate the heat and particle flux to the walls while simultaneously controlling the impurity flux into the plasma. The past several decades have witnessed the development of a comprehensive divertor strategy for ITER that combines the magnetic configuration of the standard x-point with a range of additional technologies. The current strategy is that ITER will operate with partial detachment of the strike points with vertically-oriented target plates. While an acceptable divertor strategy

may exist for ITER, it is unclear how this will project to future devices such as a Fusion Nuclear Science Facility or a DEMO reactor. Indeed, projections for a DEMO reactor suggest an unmitigated divertor heat flux of 200–300 MW [1,2]. In order to keep the heat flux at the target below the 10 MW/m^2 limit for solid materials, extreme power fractions of 90–95% may be required [3,4]. To address the potential risk that the standard divertor may not adequately project to future devices, other solutions may be needed.

In recent years, several alternative divertor concepts, referred to as advanced divertors, have been proposed as alternatives to the single x-point divertor. These concepts, such as the snowflake divertor (SFD) [5], X-divertor [6], super X-divertor [7], and x-point target divertor [8], rely upon the manipulation of the poloidal field structure in the divertor region. The snowflake divertor in particular has been the subject of studies on various devices such as TCV, NSTX, DIII-D, and EAST [9–14]. In the SFD, a second-order magnetic field null is formed by merging

together two first-order x-points. The resulting magnetic field topology has a hexagonal structure that resembles a snowflake. In actuality, one of two alternative configurations is obtained: (1) the SFD-plus with a secondary x-point in the private flux region, or (2) the SFD-minus with a secondary x-point in the scrape-off layer (SOL). The SFD-minus configuration can be further differentiated by whether the secondary x-point lies in the low-field-side (LFS) or high-field-side (HFS) SOL. A sketch of these configurations for the DIII-D tokamak is shown in Fig. 1.

One of the important outstanding issues related to the SFD is the development of reliable means for reconstructing the magnetic field structure from available diagnostic measurements. This is primarily due to the fact that the SFD forms a region of very shallow poloidal flux gradient that is difficult to resolve accurately using only external sensors. The reconstructed positions of the two closely-spaced magnetic field nulls is thus sensitive to poloidal magnetic flux measurements.It has also been quantified by Ryutov et al. [15] how small changes in the distribution of toroidal currents in the divertor region affect the resulting field structure. For example, modest changes in the divertor current density can alter the position of separatrices and x-points significantly (see Fig. 6 of [15]). This effect is especially important due to the challenges of measuring or modeling the steep edge current gradients that often exist at the plasma edge.

One of the standard and well-utilized divertor diagnostics employed on most tokamaks is infrared thermography (IRTV) which provides temporal and spatially-resolved measurements of the perpendicular heat flux on divertor surfaces. To-date, extensive use of IRTV measurements have been made to study the heat flux mitigation properties of the SFD. However, little use of the IRTV has been made to infer properties of the divertor configuration and the edge-plasma region. In this paper we present a novel technique (aimed at the identification of advanced divertor configurations such as the SFD) that employs IRTV-measured heat flux as an additional constraint on equilibrium reconstructions. This technique uses a simple iterative algorithm to infer the spatial position of the two magnetic field x-points, converging within 3–5 iterations. This technique is applied to ˜800 DIII-D SFD timeslices in order to fit new equilibria.

While the IRTV radiation signals are normally processed offline, several devices such as Tore Supra and JET have made substantial progress in developing real-time processing of thermal images [16–18]. This has enabled, for example, active feedback of radio frequency (RF)

heating based on IR measurements [16] and real-time strike point detection [17]. Due to progress in this area, one can envisage that the algorithm presented here will be amenable to include in real-time SFD controllers [19,20].

The rest of this paper is divided as follows. In Section 2, we present the algorithm that identifies the two x-point positions. The inferred x-point positions are used as a constraint to create new equilibria, which are verified to provide a better match to the measured heat flux. In Section 3, kinetic reconstructions of internal plasma profiles along with the algorithm are used to study the changes in the edge current density as the infrared constraint is applied to the x-points. In Section 4, we summarize our results and suggest avenues for future work.

2. Estimation of x-point positions via IRTV

2.1. Snowflake Minus

In the SFD-minus configuration the secondary x-point lies in the scrape-off layer. Intuitively, one can think of this x-point like a stone in a river, splitting the heat flux into multiple streams. This introduces a third peak to the heat flux profile. In DIII-D, the presence of a shelf in the divertor can also introduce additional peaks. This is a geometric effect due to the intersection of field lines with the limiter surface, and for this analysis, IRTV data in the region shadowed by the shelf is neglected. In this section we introduce a simple geometric algorithm to identify x-point positions from the heat flux peaks.

To obtain the four coordinates of the x-points we use four pieces of information available from the heat flux profile. Three degrees of freedom are set by matching three strike point positions. The strike points are easy to locate when the plasma divertor is attached, although in partially detached operation they remain somewhat detectable as determined by visual inspection of several profiles. In fully detached operation the strike points are indistinguishable (see qualitative sketch Fig. 1 of [21]). For this work we consider attached plasmas only and identify the strike points by fitting the Eich profile (eqn (1) of [22]) to the IRTV heat flux. The fourth degree of freedom is obtained by matching the relative power distribution between the two outer (inner) peaks of the SFD-minus LFS (HFS) configuration. That is, since the secondary x-point splits the heat flux into two regions, varying the x-point position within the scrape-off-layer stream also varies the power to each region. The algorithm is demonstrated for the case of SFM-minus LFS.

As shown in Fig. 2a, the mismatch in strike point location is projected perpendicular to the strike point legs. We define the error vector

$$\vec{e_1} = \left\langle \widehat{\nabla \psi_{sp_1}}, \overrightarrow{\Delta sp_1} \right\rangle \widehat{\nabla \psi_{sp_1}} \tag{1}$$

where $\langle \cdot, \cdot \rangle$ is the scalar product, $\widehat{\nabla \psi_{sp1}}$ is the unit vector in the direction of $\nabla \psi$ at strike point 1, and $\overrightarrow{\Delta sp_1}$ is the error vector between the IRTV-measured strike point location and the strike point measured from the equilibrium flux map:

$$\overrightarrow{\Delta sp_1} = \begin{bmatrix} r \\ z \end{bmatrix}_{sp_1,ir} - \begin{bmatrix} r \\ z \end{bmatrix}_{sp_1,eq} \tag{2}$$

Thus $\vec{e_1}$ is the IRTV mismatch at strike point 1, only standardized in such a way as to be independent of the orientation of the limiter surface. The error at strike point 2 is obtained analogously. The new primary x-point position is estimated from the sum of these two error vectors mapped onto flux surface vectors at the x-point. Labeling these unit vectors as $\widehat{N}_{xp1}$ and $\widehat{E}_{xp1}$ (the North and East legs at the x-point, see Fig. 2a), the change in primary x-point position is estimated

$$\Delta \overrightarrow{xp_1} = \text{sign}\left(\left\langle \vec{e_1}, \widehat{N}_{xp1} \right\rangle \right) \left| \vec{e_1} \right| \widehat{N}_{xp1} + \text{sign}\left(\left\langle \vec{e_2}, \widehat{E}_{xp1} \right\rangle \right) \left| \vec{e_2} \right| \widehat{E}_{xp1} \tag{3}$$

The intuition for this equation is that the $\vec{e_i}$ mismatches can be
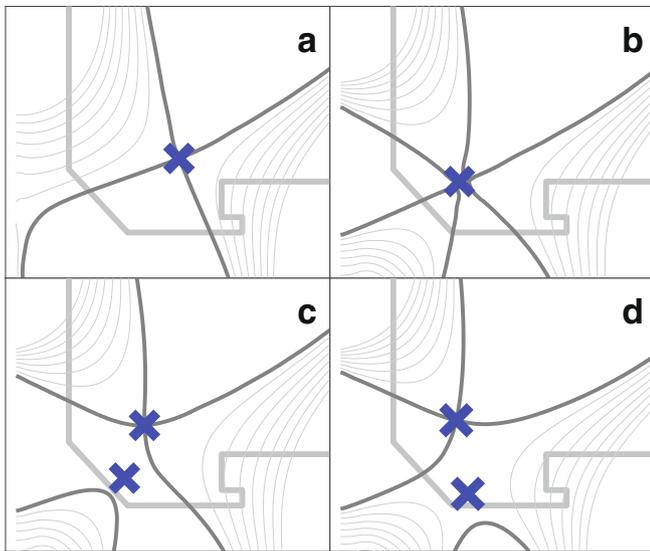
Fig. 1. (a) DIII-D standard x-point divertor configuration. (b) Perfect snowflake with a single, second-order null. (c) The snowflake-plus configuration with secondary x-point in the private flux region. (d) The snowflake-minus configuration with secondary x-point in the low-field-side scrape-off-layer.
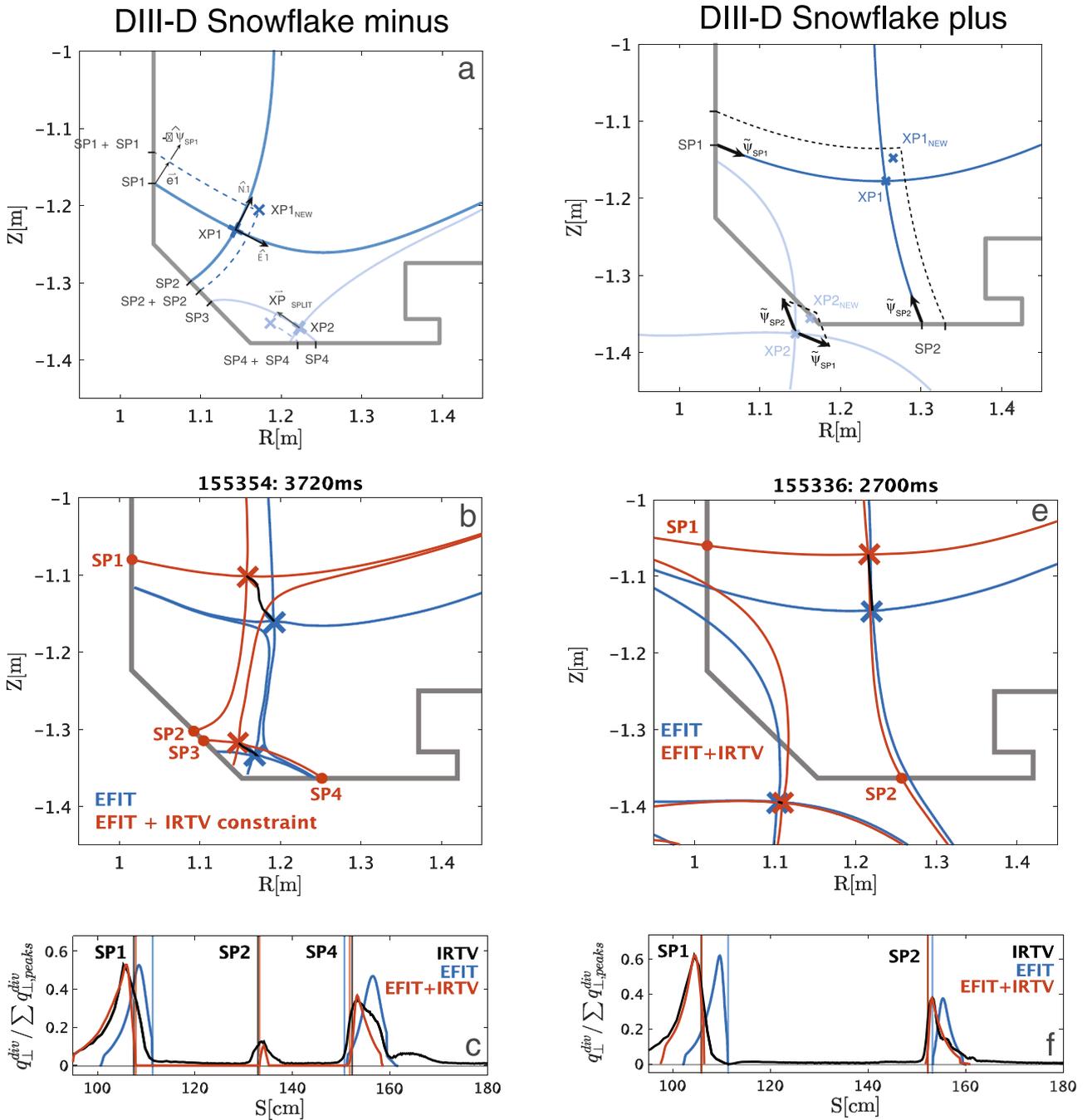
Fig. 2. (a) Geometry definitions used in the snowminus x-point algorithm. (b) Original EFIT equilibrium (blue) and converged equilibrium (orange) from applying the IRTV constraint. Convergence path of the x-points is shown in black. The EFIT equilibrium is a snowflake plus, although the IRTV heat flux signature (fig. 2c, black) has 3 heat flux peaks characteristic of the snowflake minus. (c) Measured (black) and simulated (blue, orange) heat flux profiles. (d), (e), and (f) Same as a, b, c but for the snowflake plus configuration. (For interpretation of the references to colour in this figure legend, the reader is referred to the web version of this article.)

mostly compensated for by orthogonal translation of the strike point leg. The terms $|\vec{e}_i|$ indicate the magnitude of the step, and the remaining terms indicate the direction. It was found during testing that first mapping the error to the x-point, i.e., moving in the direction of $\widehat{N}_{xp1}$ and $\widehat{E}_{xp1}$ instead of $\vec{e}_1$ and $\vec{e}_2$, was more robust in obtaining a converged solution.

The assumption used in this approach is that the overall field structure of the divertor is preserved– translation of flux surfaces near the strike point is highly correlated with translation of the same surface near the x-point, so that the strike point mismatch is not primarily caused by modified curvature in the strike point leg. This assumption

was verified empirically. When snowflake-plus equilibria were obtained by constraining the strike points (instead of the x-points), the x-points were translated to nearly the same position. This indicates it was less costly for the free-boundary equilibrium solver to satisfy strike point constraints by also translating the x-points and not adding curvature into the strike legs. This may be aided by the fact that the DIII-D divertor are not particularly long. In longer-legged divertors, the effect of modified curvature in the strike legs would become more important and could account for a larger fraction of the strike point discrepancies.

The position of the secondary x-point is obtained from matching strike point 4 and the power splitting between the middle and outer peaks, denoted $\Delta xp_{2,split}$. To determine $\Delta xp_{2,split}$ the power at each peak is

measured by integrating the IRTV-based heat flux with $P_i = \int_{pk,i} 2\pi R(S) q_\perp^{div} dS$. The power-sharing between peaks is also related to the exponentially-decaying heat flux profile at the midplane, which gives the power fraction expression:

$$\frac{P_4}{P_2 + P_4} = \frac{\int_{r_{split}}^{\infty} q_\perp^{mid,peak} e^{-r/\lambda_q^{eff}} dr}{\int_0^{\infty} q_\perp^{mid,peak} e^{-r/\lambda_q^{eff}} dr} \tag{4}$$

$$= e^{-r_{split}/\lambda_q^{eff}}$$

where P_2 and P_4 are the power levels associated with the peaks at strike point 2 (middle peak) and strike point 4 (outer peak), r is the radial position relative to the radius of the outer midplane separatrix $r = R - R_{mid}$, r_{split} is the midplane radial position of the secondary separatrix which divides heat flux between the two regions, and λ_q^{eff} is the effective power-decay length used for power splitting. A common method for obtaining the power-decay length is to fit the Eich profile [22] to the heat flux at the outer strike point. However, previous results from TCV [23] suggest that for the SFD, there is higher transport in the SOL intra-null region than in the far SOL. This results in a significantly larger effective decay length for power-splitting, λ_q^{eff}, than is obtained by the Eich fit to SP4.

To obtain λ_q^{eff}, we use the original EFIT01 equilibria from a subset of shots that each have a wide range of mid-plane separation between the primary and secondary separatrices, r_{split}. The power fraction is obtained from the IRTV, and λ_q^{eff} is then obtained by fitting to a slightly-modified Eq. (4).

$$\frac{P_4}{P_2 + P_4} = e^{-(r_{split} + r_{shift})/\lambda_q^{eff}} \tag{5}$$

The fit is shown in Fig. 3. The variable r_{shift} is an additional fitting parameter included to accommodate any bias errors in the equilibrium reconstruction. We find that $\lambda_q^{eff} = 5.6$mm, and fitting the Eich profile to SP4 we had found $\lambda_q^{SP4} = 1.9$mm. This is an increase factor of 2.9 betweeen the λ_q and comparable to the 2.4 increase factor in TCV [23].

When λ_q^{eff} is obtained, Eq. 4 can be used to obtain the secondary separatrix postion, which defines a target flux coordinate of the secondary x-point $\psi_{xp2,targ} = \psi(R_{mid} + r_{split}, Z_{mid})$. We note that the
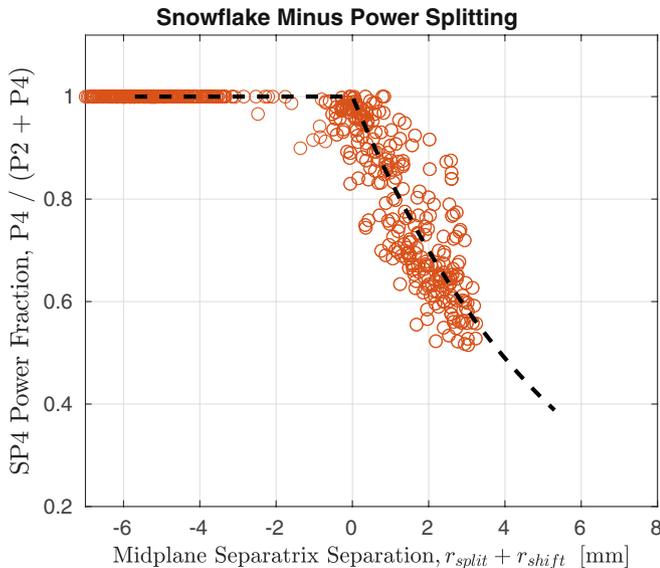
secondary x-point distorts the flux surfaces directly around itself, so we do not specify directly that the x-point lie on the $\psi_{xp2,targ}$ flux surface of the current iteration of equilibrium. Instead, we update using

$$\overrightarrow{\Delta xp_{2,split}} = \left(\psi_{xp2} - \psi_{xp2,targ} \right) \left| \nabla \psi_{midplane} \right|^{-1} \left\langle f_{exp} \right\rangle \widehat{E}_{xp2} \tag{6}$$

which is not sensitive to the local flux surface distortion. ψ_{xp_2} is the flux label associated with the secondary x-point, $\nabla \psi_{midplane}$ is the flux gradient at the outer midplane, $\langle f_{exp} \rangle$ is the flux expansion averaged over the divertor region, and $\widehat{E}_{xp2}$ is the East leg unit vector at xp_2. Total movement of the secondary x-point is then

$$\Delta \overrightarrow{xp_2} = \text{sign}\left(\left\langle \overrightarrow{e_4}, \widehat{N}_{xp2} \right\rangle \right) \left| \overrightarrow{e_4} \right| \widehat{N}_{xp2} + \overrightarrow{\Delta xp_{2,split}} \tag{7}$$

This algorithm is employed in an iterative procedure. First, the SP1 and SP4 strike point positions are inferred from IRTV by fitting the Eich profile [22]. The position of SP2 is inferred as the position where the heat flux is 2/3 magnitude of the heat flux peak. This heuristic is appropriate so long as the left-half peak width of SP2 is much less than the strike point mismatch, a condition which is met by an order of magnitude. There is also some concern that $E \times B$ drifts can affect the power deposition profile [24–26]. In-depth analysis of $E \times B$ drift is beyond the scope of this paper, but we note that some of the evidence for enhanced drift such as double-peaked heat profiles, and asymmetry in the middle strike points is not present for these DIII-D shots. Additionally, the shots were run with reverse B_T, i.e. with the ion $\boldsymbol{B} \times \nabla B$ drift away from the lower divertor. At SP1, this results in $E \times B$ drift downwards, when in fact for a majority of equilibria, the power deposition was higher than predicted by the equilibrium flux map.

Once the strike points and power fraction are obtained from IRTV, Eq. 3, are used to update the x-point positions. Using the TokSys [27] suite of software, we create a new equilibrium using the previous equilibrium as an input. The IRTV-inferred x-point positions are used as a constraint, while differences between the new and previous equilibria are penalized using a weighted sum of squares. The penalized differences include the position of the plasma boundary at a number of points, poloidal beta β_p, internal inductance L_i, plasma current I_p, and currents in the poloidal field coils (F-coils and E-coil). This process repeats several times until the x-points and equilibria converge.

An example convergence path for SFD-minus is shown in Fig. 2b. In this case the magnetics-only reconstruction from EFIT [28] presents a SFD-plus configuration (blue). The secondary x-point lies inside the private flux region. However, the heat flux indicates the equilibrium should be a SFD-minus configuration as evidenced by the presence of a third heat flux peak (Fig. 2c). The primary and secondary x-points are inferred to be located further upwards and outwards by 4.1 cm and 4.2 cm respectively. The new flux map is a SFD-minus configuration as expected.

The heat flux simulation is shown in Fig. 2c and was obtained using the SFD heat diffusion model described in [29]. The model explicitly evolves a heat equation for diffusion across fieldlines, with consideration of the large connection length gradients present in the SFD, and in multiple distinct regions defined by the SFD topology. The simulated heat flux for this equilibrium is in much better agreement with the IRTV heat flux. On average for the SFD-minus configuration, the combined strike point mismatch in the divertor is reduced from 9.4 cm to 0.9 cm and the power distribution error is reduced from 15% to 2%.

2.2. Snowflake plus

In the SFD-plus configuration, the secondary x-point lies in the private flux region so that the divertor heat flux has only two heat flux peaks. The system is overdetermined in the sense that the heat flux mismatch at two strike points will be accounted for by four parameters–the (r,z) coordinates of the two x-points. A simple option is to

Fig. 3. The fraction of outboard power deposited at strike point 4. The dashed line gives the fitted value $\lambda_q^{eff} = 5.6$mm.

constrain the equilibrium using the inferred strike point positions vice x-point positions. However, for consistency with the SFD-minus scenario, we present an x-point algorithm for SFD-plus. Consistency would be useful, for example, if a real-time reconstruction algorithm were configured to receive x-point positions as a virtual diagnostic. For both methods, the final strike point positions match the IRTV strike points, and the x-points are in good agreement with each other. As shown in Fig. 4, the x-point model presented here obtains similar results while moving the x-points slightly less distance (mean 7.3 cm vs 6.3 cm).

A description of the x-point finder is as follows. First, we assign weights on the movements $w_{xp1,sp1}, w_{xp2,sp1}, w_{xp1,sp2}$ and $w_{xp2,sp2}$ indicating how much to move the primary and secondary x-points to account for mismatch at the 1st and 2nd strike points. There is some flexibility in assigning weights, but the combination $w_{xp1,sp1} = 0.9, w_{xp2,sp1} = 0.1,$ $w_{xp1,sp2} = 0.3, w_{xp2,sp2} = 0.7$ was found to give satisfactory results, matching the strike points exactly with minimal movement of the x-points. Similar to Eq. 3, the primary x-point is found as

$$\Delta \overrightarrow{xp_1} = w_{xp1,sp1}\text{sign}\left(\left\langle \overrightarrow{e_1}, \widehat{N}_{xp1} \right\rangle\right)\left|\overrightarrow{e_1}\right|\widehat{N}_{xp1} + w_{xp1,sp2}\text{sign}\left(\left\langle \overrightarrow{e_2}, \widehat{E} \right\rangle\right)\left|\overrightarrow{e_2}\right|\widehat{E}_{xp1} \tag{8}$$

For the secondary x-point, we first define the vectors $\widetilde{\psi}_{sp_1}$ and $\widetilde{\psi}_{sp_2}$, oriented along the strike point legs as shown in Fig. 2d with magnitude equal to the error in strike point positions. Reasoning by example, when xp_2 is perturbed parallel to the strike point leg $\widetilde{\psi}_{sp_2}$, the strike point moves outwards. When xp_2 is perturbed orthogonally, the strike point stays roughly constant. This behavior was verified for a large number of equilibria. Thus, to update xp_2 we use a combination of movement parallel and perpendicular to the strike point legs:

$$\Delta \overrightarrow{xp_2} = w_{xp2,sp2}\widetilde{\psi}_{sp_2} + w_{xp2,sp1}\left\langle \widetilde{\psi}_{sp_1}, \widehat{\nabla\psi}_{sp_2} \right\rangle\widehat{\nabla\psi}_{sp_2} \tag{9}$$

The result of this algorithm for SFD-plus is shown in Fig. 2d with the heat flux simulation in Fig. 2e. The new heat flux profile shows much better agreement with IRTV. On average for SFD-plus, the strike points move a combined 5.4 cm to fully correct the mismatch.

3. Profile and diagnostic analysis

3.1. Profile analysis and edge current

The bootstrap current is an important factor for confinement and stability of the plasma and has been shown to have a significant effect on geometry in the SFD [15]. Experimentally, bootstrap current at the edge is a difficult quantity to measure and significant effort has been devoted to developing accurate models [30–33]. Additionally, modelling and experiments of the SFD indicate several differences in the edge including increased shear and edge current leading to improved pedestal stability [34–36]. In this section, we evaluate profile changes to the bootstrap current as the shape is modified by the IRTV constraint. We first use the Consistent Automatic Kinetic Equilibria (CAKE) [37] tool to generate kinetic equilibria. These are converted to TokSys format where we then apply the shape constraints. In the timeslices analyzed the equilibria are H-mode SFD (plus or minus) and the average peak edge current is 0.78 MA/m^2. We apply the x-point constraints to the equilibria and measure the change in peak edge current with sample profiles shown in Fig. 5. The changes in edge current have a mean 16% reduction in j_{boot} with 12% standard deviation. Fig. 6 indicates a simple relationship (explained variance 85%) between the change in x-points and edge current as found by linear regression. Here, Δj_{true} refers to the change in edge current before and after applying the IRTV constraints as found from the Grad-Shafranov fit, while $\Delta j_{predict}$ is the regression estimate. The weights on the x-point positions rx_1, rx_2, zx_1 and zx_2 for SFD-minus and plus are $\begin{bmatrix} -2.7 & -3.0 & -0.6 & 0.5 \end{bmatrix}$ and $\begin{bmatrix} -5.5 & 0.0 & -0.1 & 2.3 \end{bmatrix}$ MA/m^2/cm respectively. The most important parameters are the radial positions of both x-points (SFD-minus) or radius of the primary x-point only (SFD-plus). These results suggest that accurately resolving SFD shape is an important factor for determining the distribution of toroidal edge currents.

Some speculative analysis compared electron temperature (T_e) and density (n_e) profiles in the IRTV-constrained and unconstrained cases, and found that the profiles tended to shift outward, improving profile alignment with the separatrix. However, the direction of the shift and improvement of alignment was not consistent across all studied time slices. These results come with a caveat that the constraints were applied within the TokSys software framework which has several limitations and capabilities compared to the EFIT and kinetic EFIT codes in the ability to match diagnostics and profiles. An attempt to match all diagnostic inputs available was not made. For stronger-founded comparisons, future work will focus on implementing the IRTV diagnostic directly into the EFIT and kinetic EFIT solvers for integrated solutions including more of the relevant diagnostics. Fig. 7 depicts the example of diagnostic fitting tradeoff in TokSys for shot 155354 where the original equilibrium incorrectly predicted a snowflake-plus configuration (see Fig. 2b). As the weight on IRTV measurements increases, the magnetic probe errors increase by a factor of 2.5. However, an IRTV weight of 0.45 results in only a 30% increase of magnetic probe error and is sufficient to correct the mismatch in snowflake type. The fitting weight is only directly applied to the x-points so that Δxp is driven to zero. The fact that Δsp, the summed strike point errors, and $\Delta\psi$, the flux at the secondary x-point via Eq. 7, converge to zero along with Δxp is evidence that the algorithm has identified the correct x-points. The increase in strike point error before the transition to SFD-minus is due to interactions between the primary and secondary separatrices.

Fig. 4. Total distance moved by the x-points in the snowflake plus configuration when constraining the strike point positions only, versus constraining the x-points via Eq. 8.
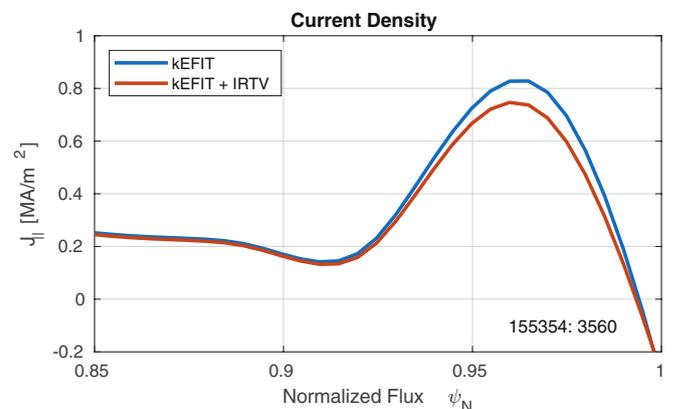
Fig. 5. Change in the parallel edge current density as the IRTV constraint is applied.
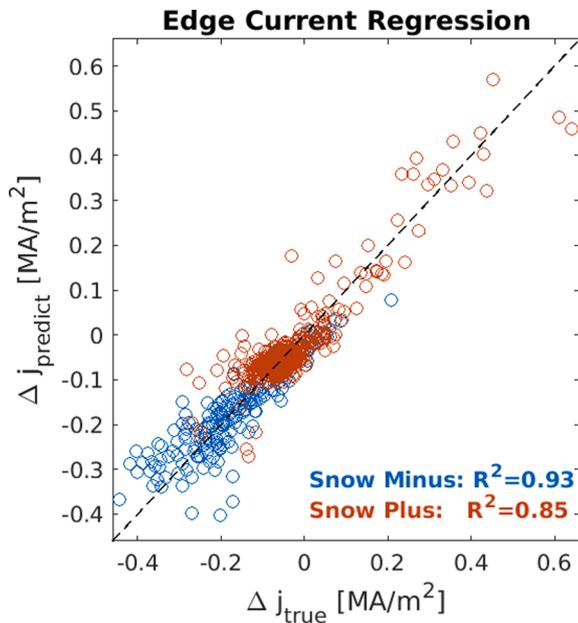
Fig. 6. Linear regression estimates for the change in the equilibrium edge current using the movement of x-points as predictor variables.
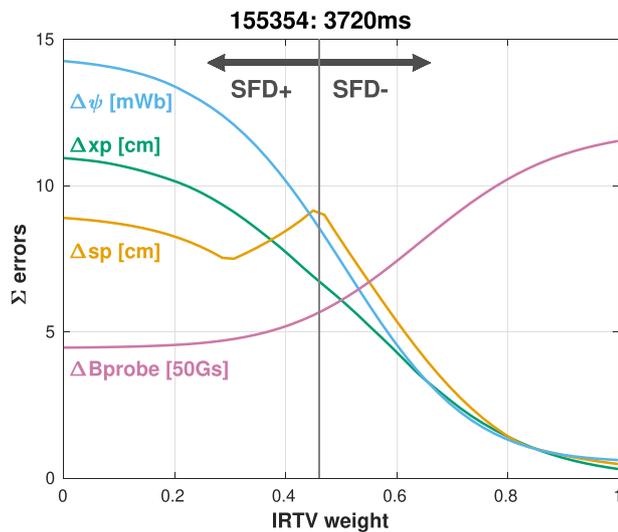
Fig. 7. Equilibrium fitting tradeoff for DIII-D 155354, the same example as shown in Fig. 2b, between the magnetic probe errors and the IRTV-inferred characteristics: strike point positions, flux of the secondary x-point, and x-point positions.

4. Conclusion

We have developed a technique to improve equilibrium reconstruction in the snowflake divertor (SFD) using heat flux from the IRTV diagnostic. Strike point positions from the heat flux and power splitting between peaks are used to infer the two x-point positions, which can be used a virtual diagnostic to supplement the fit from magnetic diagnostics. Heat flux profiles for the newly-fitted equilibria show much better agreement with IRTV-measured heat flux as strike point errors are reduced from a summed average 9.4 cm to 0.9 cm. Changes in the x-point positions are strongly correlated with changes in the edge current. A subject of further study is to include this x-point diagnostic directly into kinetic equilibria reconstructions to further elucidate structure of the pedestal in snowflake minus and plus configurations.

Disclaimer

This report is prepared as an account of work sponsored by an agency of the United States Government. Neither the United States Government nor any agency thereof, nor any of their employees, makes any warranty, express or implied, or assumes any legal liability or responsibility for the accuracy, completeness, or usefulness of any information, apparatus, product, or process disclosed, or represents that its use would not infringe privately owned rights. Reference herein to any specific commercial product, process, or service by trade name, trademark, manufacturer, or otherwise, does not necessarily constitute or imply its endorsement, recommendation, or favoring by the United States Government or any agency thereof. The views and opinions of authors expressed herein do not necessarily state or reflect those of the United States Government or any agency thereof.

CRediT authorship contribution statement

J.T. Wai: Conceptualization, Methodology, Software, Writing - original draft. **P.J. Vail:** Conceptualization, Methodology, Software, Writing - original draft. **A.O. Nelson:** Investigation, Validation, Writing - review & editing. **Z.A. Xing:** Investigation, Conceptualization. **C. Lasnier:** Data curation, Resources. **E. Kolemen:** Conceptualization, Supervision, Funding acquisition, Writing - review & editing.

Declaration of Competing Interest

The authors declare that they have no known competing financial interests or personal relationships that could have appeared to influence the work reported in this paper.

Acknowledgements

References

[1] J. You, et al., Conceptual design studies for the european DEMO divertor: Rationale and first results, Fusion Eng. Des. 109–111 (2016) 1598–1603, https://doi.org/10.1016/j.fusengdes.2015.11.012.

[2] N. Asakura, et al., Studies of power exhaust and divertor design for a 1.5 GW-level fusion power DEMO, Nucl. Fusion 57 (2017), 126050, https://doi.org/10.1088/1741-4326/aa867a.

[3] M. Kotschenreuther, et al., On heat loading, novel divertors, and fusion reactors, Phys. Plasmas 14 (2007), https://doi.org/10.1063/1.2739422.

[4] M. Wischmeier, High density operation for reactor-relevant power exhaust, J. Nucl. Mater. 463 (2015) 22–29, https://doi.org/10.1016/j.jnucmat.2014.12.078.

[5] D.D. Ryutov, Geometrical properties of a "snowflake divertor, Phys. of Plasmas 14 (2007), https://doi.org/10.1063/1.2738399.

[6] M. Kotschenreuther, et al., Magnetic geometry and physics of advanced divertors: The x-divertor and the snowflake, Phys. Plasmas 20 (2013), 102507, https://doi.org/10.1063/1.4824735.

[7] P.M. Valanju, et al., Super-x divertors and high power density fusion devices, Phys. Plasmas 16 (2009), https://doi.org/10.1063/1.3110984.

[8] M. Umansky, et al., Assessment of x-point target divertor configuration for power handling and detachment front control, Nucl. Mater. Energy 12 (2017), https://doi.org/10.1016/j.nme.2017.03.015.

[9] F. Piras, et al., Snowflake divertor experiments on TCV, Plasma Phys. Controlled Fusion 52 (2010), https://doi.org/10.1088/0741-3335/52/12/124010.

[10] V.A. Soukhanovskii, et al., Snowflake divertor configuration studies in national spherical torus experiment, Phys. Plasmas 19 (2012), https://doi.org/10.1063/1.4737117.

[11] E. Kolemen, et al., Heat flux management via advanced magnetic divertor configurations and divertor detachment, J. Nucl. Mater. 463 (2015), https://doi.org/10.1016/j.jnucmat.2014.11.099.

[12] B. Xiao, et al., Enhancement of EAST plasma control capabilities, Fusion Eng. Des. 112 (2016), https://doi.org/10.1016/j.fusengdes.2016.06.004.

[13] B. Labit, et al., Experimental studies of the snowflake divertor in TCV, Nucl. Mater. Energy 12 (2017) 1015–1019, https://doi.org/10.1016/j.nme.2017.03.013.

[14] V. Soukhanovskii, et al., Developing physics basis for the snowflake divertor in the DIII-d tokamak, Nucl. Fusion 58 (2018), https://doi.org/10.1088/1741-4326/aaa6de.

[15] D.D. Ryutov, M.A. Makowski, M.V. Umansky, Local properties of the magnetic field in a snowflake divertor, Plasma Phys. Controlled Fusion 52 (2010), 105001, https://doi.org/10.1088/0741-3335/52/10/105001.

[16] P. Moreau, et al., RF heating optimization on tore supra using feedback control of infrared measurements, Fusion Eng. Des. 82 (2007) 1030–1035, https://doi.org/10.1016/j.fusengdes.2007.01.022.

[17] G. Vagliasindi, et al., Application of cellular neural network methods to real time image analysis in plasma fusion, in: 2007 IEEE International Symposium on Intelligent Signal Processing, IEEE, 2007. doi: 10.1109/wisp.2007.4447505.

[18] D. Alves, et al., Vessel thermal map real-time system for the JET tokamak, Phys. Rev. Special Topics – Accelerators Beams 15 (2012), https://doi.org/10.1103/physrevsTable 15.054701.

[19] E. Kolemen, et al., Initial development of the DIII–d snowflake divertor control, Nucl. Fusion 58 (2018), https://doi.org/10.1088/1741-4326/aab0d3.

[20] P.J. Vail, et al., Design and simulation of the snowflake divertor control for NSTX–u, Plasma Phys. Controlled Fusion 61 (2019), https://doi.org/10.1088/1361-6587/aaf94a.

[21] A. Kallenbach, et al., Partial detachment of high power discharges in ASDEX upgrade, Nucl. Fusion 55 (2015), 053026, https://doi.org/10.1088/0029-5515/55/5/053026.

[22] T. Eich, et al., Scaling of the tokamak near the scrape-off layer h-mode power width and implications for ITER, Nucl. Fusion 53 (2013), https://doi.org/10.1088/0029-5515/53/9/093031.

[23] R. Maurizio, C. Tsui, B. Duval, H. Reimerdes, C. Theiler, J. Boedo, B. Labit, U. Sheikh, M. Spolaore, The effect of the secondary x-point on the scrape-off layer transport in the TCV snowflake minus divertor, Nucl. Fusion 59 (2018), 016014, https://doi.org/10.1088/1741-4326/aaee1b.

[24] A.V. Chankin, G. Corrigan, S.K. Erents, G.F. Matthews, J. Spence, P.C. Stangeby, Possible explanation for doubly peaked profiles at the divertor target in JET, Plasma Phys. Controlled Fusion 43 (2001) 299–304, https://doi.org/10.1088/0741-3335/43/3/305.

[25] V. Rozhansky, P. Molchanov, I. Veselova, S. Voskoboynikov, A. Kirk, D. Coster, Contribution of exb drifts and parallel currents to divertor asymmetries, Nucl. Fusion 52 (2012), 103017, https://doi.org/10.1088/0029-5515/52/10/103017.

[26] G. Canal, T. Lunt, H. Reimerdes, B. Duval, W.V. Vijvers, Enhanced exb drift effects in the tcv snowflake divertor, Nuclear Fusion 55 (2015) 123023, https://doi.org/10.1088/0029-5515/55/12/123023.

[27] M.L. Walker, et al., Development environments for tokamak plasma control, in, in: IEEE 26th Symposium on Fusion Engineering (SOFE), IEEE, 2015, https://doi.org/10.1109/sofe.2015.7482289.

[28] L. Lao, et al., Reconstruction of current profile parameters and plasma shapes in tokamaks, Nucl. Fusion 25 (1985), https://doi.org/10.1088/0029-5515/25/11/007.

[29] P. Vail, O. Izacard, E. Kolemen, Optimization of the snowflake divertor for power and particle exhaust on NSTX–u, Nucl. Mater. Energy 19 (2019) 516–523, https://doi.org/10.1016/j.nme.2019.03.003.

[30] S. Koh, et al., Bootstrap current for the edge pedestal plasma in a diverted tokamak geometry, Phys. Plasmas 19 (2012), https://doi.org/10.1063/1.4736953.

[31] E.A. Belli, et al., Limitations of bootstrap current models, Plasma Phys. Controlled Fusion 56 (2014), https://doi.org/10.1088/0741-3335/56/4/045006.

[32] R. Hager, C.S. Chang, Gyrokinetic neoclassical study of the bootstrap current in the tokamak edge pedestal with fully non-linear coulomb collisions, Phys. Plasmas 23 (2016), https://doi.org/10.1063/1.4945615.

[33] D.M. Thomas, et al., Measurement of edge currents in DIII-d and their implication for pedestal stability, Phys. Plasmas 12 (2005), 056123, https://doi.org/10.1063/1.1879992.

[34] D.D. Ryutov, et al., A snowflake divertor: a possible solution to the power exhaust problem for tokamaks, Plasma Phys. Controlled Fusion 54 (2012), https://doi.org/10.1088/0741-3335/54/12/124050.

[35] S.Y. Medvedev, et al., Edge stability and pedestal profile sensitivity of snowflake diverted equilibria in the TCV tokamak, Contrib. Plasma Phys. 50 (2010), https://doi.org/10.1002/ctpp.201010053.

[36] M. Umansky, et al., Edge plasma in snowflake divertor, Contrib. Plasma Phys. 50 (2010), https://doi.org/10.1002/ctpp.201010057.

[37] Z.A. Xing, D. Eldon, E. Kolemen, et al., CAKE: Consistent automatic kinetic equilibrium reconstruction, manuscript in preparation for FED (2020).

[38] O. Meneghini, et al., Integrated modeling applications for tokamak experiments with OMFIT, Nucl. Fusion 55 (2015), https://doi.org/10.1088/0029-5515/55/8/083008.